

Raman spectroscopy and X-ray diffraction of sp^3 -CaCO₃ at lower mantle pressures

Sergey S. Lobanov^{1,2}, Xiao Dong³, Naira S. Martirosyan^{1,2}, Artem I. Samtsevich⁴, Vladan Stevanovic⁵, Pavel N. Gavryushkin^{2,6}, Konstantin D. Litasov^{2,6}, Eran Greenberg⁷, Vitali B. Prakapenka⁷, Artem R. Oganov^{4,8,9,10}, and Alexander F. Goncharov^{1,11}

¹Geophysical Laboratory, Carnegie Institution of Washington, Washington, DC 20015, USA

²Sobolev Institute of Geology and Mineralogy Siberian Branch Russian Academy of Sciences, 3 Pr. Ac. Koptyga, Novosibirsk 630090, Russia

³Center for High Pressure Science and Technology Advanced Research, Beijing 100193, China

⁴Skolkovo Institute of Science and Technology, Skolkovo Innovation Center, 5 Nobel St., Moscow 143026, Russia

⁵Department of Metallurgical and Materials Engineering, Colorado School of Mines, Golden, CO 80401, USA

⁶Novosibirsk State University, Novosibirsk 630090, Russian Federation

⁷Center for Advanced Radiation Sources, University of Chicago, Chicago, IL 60632, USA

⁸Moscow Institute of Physics and Technology, 9 Institutskiy Lane, Dolgoprudny City, Moscow Region 141700, Russia

⁹School of Materials Science, Northwestern Polytechnical University, Xi'an 710072, China

¹⁰Department of Geosciences, Center for Materials by Design, Institute for Advanced Computational Science, Stony Brook University, Stony Brook, New York 11794, United States

¹¹Key Laboratory of Materials Physics, Institute of Solid State Physics CAS, Hefei 230031, China

*E-mail: slobanov@carnegiescience.edu; slobanov@igm.nsc.ru

Abstract

The exceptional ability of carbon to form sp^2 and sp^3 bonding states leads to a great structural and chemical diversity of carbon-bearing phases at non-ambient conditions. Here we use laser-heated diamond anvil cells combined with synchrotron x-ray diffraction, Raman spectroscopy, and first-principles calculations to explore phase transitions in CaCO₃ at $P > 40$ GPa. We find that post-aragonite CaCO₃ transforms to the previously predicted $P2_1/c$ -CaCO₃ with sp^3 -hybridized carbon at 105 GPa (~ 30 GPa higher than the theoretically predicted crossover pressure). The lowest enthalpy transition path to $P2_1/c$ -CaCO₃ includes reoccurring sp^2 - and sp^3 -CaCO₃ intermediate phases and transition states, as revealed by our variable-cell nudged elastic band simulation. Raman spectra of $P2_1/c$ -CaCO₃ show an intense band at 1025

cm⁻¹, which we assign to the symmetric C-O stretching vibration based on empirical and first principles calculations. This Raman band has a frequency that is ~20 % lower than the symmetric C-O stretching in *sp*²-CaCO₃, due to the C-O bond length increase across the *sp*²-*sp*³ transition, and can be used as a fingerprint of tetrahedrally-coordinated carbon in other carbonates.

Key words

Calcite; aragonite; carbonates; high pressure; *sp*³-carbon; crystal structure;

Introduction

The thermodynamic ground state of carbon at ambient conditions is graphite with a triangular bonding pattern (*sp*² hybridization). High pressure (P), however, favors tetrahedrally-bonded (*sp*³) carbon, and diamond is stable at P > 1.7 GPa (0 K) [1]. The different bonding patterns of graphite and diamond result in very different mechanical, optical, electric, and thermal properties [2], making carbon a truly remarkable element. On top of this, the binding energy between carbon atoms is very large leading to high melting temperatures (T) as well as high activation energies for the solid state phase transitions [1]. As a result, carbon has a rich variety of metastable phases with mixed *sp*² and *sp*³ bonding patterns that may integrate the unique physical properties of both graphite and diamond [3,4]. The synthesis of such novel carbon-based technological materials requires navigating in the carbon energy landscape as well as insights into the trajectories and mechanisms of its phase transitions [5].

Unlike carbon, the thermodynamically stable form of silicon at ambient condition has the cubic diamond structure. Not surprisingly, nearly all low-pressure silicates incorporate silicon exclusively in the form of *sp*³-hybridized SiO₄ tetrahedral groups. The electronic structure of SiO₄-tetrahedra is such that each oxygen has a half-occupied *p* orbital available for polymerization with adjacent groups. The topology of polymerized SiO₄-networks largely governs the physical properties of silicates and serves as the basis for their structural classification [6,7]. On the other hand, *sp*²-hybridized CO₃ triangular groups have an additional C-O π bond, and as a result, are isolated in the crystal structures of carbonates. This difference in the electronic structures of CO₃ and SiO₄ groups leads to very different physical properties of *sp*²-carbonates and *sp*³-silicates. At high pressure, however, the electronic structure of carbon in carbonates may change via the C-O π bond polymerization as individual CO₃ groups approach each other. Theoretical computations predict that *sp*³-carbonates become thermodynamically stable at P > ~ 80-130 GPa [8-12]. Here we investigate the high-P behavior of CaCO₃, one of the

most abundant carbonates near the Earth's surface and a good proxy for carbonate chemical composition in the mantle [13,14].

Previous high-P studies have revealed a number of pressure-induced transformations in CaCO_3 . At $P < \sim 40$ GPa, (meta)stable phases of CaCO_3 include calcite, aragonite, CaCO_3 -II, CaCO_3 -III, CaCO_3 -IIIb, and CaCO_3 -VI (e.g. [9,15-17]). At $P > 40$ GPa, CaCO_3 transforms into post-aragonite, which has been reported as a stable phase up to 137 GPa [9,18,19]. Importantly, all these structures contain sp^2 -hybridized carbon forming triangular CO_3 groups. Pyroxene-like $C222_1$ - CaCO_3 , which has been predicted stable at $P > 137$ GPa, has a different bonding pattern with sp^3 -hybridized carbon forming polymerized CO_4 -chains [9]. This prediction gained some experimental support in that the major Bragg peaks of the $C222_1$ - CaCO_3 had been observed in experiment at $P > 140$ GPa [19]. The high synthesis pressure implied that sp^3 - CaCO_3 is not present in the Earth's mantle (135 GPa is the core-mantle boundary pressure) and further experimental studies of sp^3 -carbonates were shifted to other compositions. More recently, the sp^2 - sp^3 transition in CaCO_3 was revisited by Pickard and Needs [12] who predicted a new sp^3 - CaCO_3 phase ($P2_1/c$) at $P > 76$ GPa calling for a new synthesis study.

Here we explore phase transitions in CaCO_3 at $P > 40$ GPa via synchrotron x-ray diffraction, Raman spectroscopy, and first-principles calculations. We establish the stability field of sp^3 -bonded $P2_1/c$ - CaCO_3 and show that this phase has a strong Raman band characteristic of fourfold carbon in its crystal structure. We provide computational insights into the sp^2 - sp^3 phase transition mechanism, which in CaCO_3 appears to be a complex multistage process. Finally, our results support the notion of the effect of sp^2 - sp^3 crossover on the carbonates crystal chemistry in the lower mantle.

Methods

Experimental methods. Diamond anvil cells (DACs) equipped with flat 200-300 μm culets were used to generate high pressure. Rhenium gaskets (~ 200 μm thick) were indented to ~ 30 -40 μm by the anvils and laser-drilled in the center of the indentation in order to prepare a sample chamber with a diameter of 70-120 μm . The sample chamber was loaded with 99.95 % CaCO_3 (Alfa Aesar) mixed with Pt powder (20-30 %) which served both as a heating laser absorber and as a pressure standard [20]. No pressure-transmitting medium was used in the experiments.

X-ray diffraction (XRD) measurements and laser-heatings were performed at the 13ID-D GeoSoilEnviroCARS beamline (Argonne National Lab, APS) that allows *in situ* XRD collections at extreme P-T conditions and a subsequent high resolution mapping of the sample quenched to ambient temperature [21]. At all pressures a typical heating cycle involved: (i) heating to $T \sim 2000$ K, while following the diffraction pattern each 100-200 K; (ii) annealing at

T ~ 2000 K, at which temperature we typically observed the formation of new XRD peaks, while moving the samples by ~ 10 μm in horizontal and vertical directions (1 μm step); (iii) quenching and mapping the heated region in order to find areas with less Pt and more CaCO_3 . The x-ray energy was 37-42 keV focused to ~ 3 by 4 μm spot. 2D XRD images were integrated using the Dioptas software [22] for on-line analyses. Selected XRD patterns were analyzed in PowderCell 2.4 and LeBail-refined in GSAS/EXPGUI [23,24]. Equation of state fitting (EOS) was performed using EoSFit7GUI [25] and VESTA [26] for structure visualization.

After the synthesis and XRD measurements, samples with sp^3 - CaCO_3 were characterized by Raman spectroscopy upon decompression at the Geophysical Laboratory using solid-state 488 (Spectra-Physics), 532 (Laser Quantum GEM), and 660 nm (Laser Quantum Ignis) laser-excitations focused to a 3-4 μm spot size in diameter. The use of three excitation wavelengths allows unambiguously identifying bands that are Raman in origin. Backscattered Raman radiation was spatially filtered through a 50 μm pinhole (magnified by 10 using a Mitutoyo 20X NA0.4 long working length objective lens) to eliminate spurious signal and collected by custom Raman spectrometers with CCD array detectors (PIXIS 100, Princeton Instruments) equipped with same-turret 300 and 1200/1500 grooves per mm gratings (HR 460, JOBIN YVON for the 488 nm setup and Acton SP2300/2500 of Princeton Instruments for 532 nm 660 nm, respectively). The spectral resolution was ~ 4 cm^{-1} . The diamond Raman edge stress scale [27] was used to determine pressure on decompression with an uncertainty of ~ 3-5 GPa.

Theoretical methods

In this study we relied on the previous structural searches [12] but the use of USPEX yields similar results (not presented here). Structural relaxations and Raman intensity calculations were performed based on the density functional theory (DFT) as implemented in the Quantum-ESPRESSO code [28]. The norm conserving pseudopotential [29] was used and the electron-electron exchange and correlation was described by the local density approximation (LDA) exchange-correlation functional of Ceperley and Alder, as parameterized by Perdew and Zunger (CA-PZ) [30]. The plane-wave cutoff energy with 250 Ry, and a k-point spacing ($2\pi \times 0.03 \text{ \AA}^{-1}$) was used to generate Monkhorst-Pack k-points grids for Brillouin zone sampling [31].

Results and Discussion

X-ray diffraction. Room-temperature compression to $P > 40$ GPa results in a diffraction pattern with several low intensity diffuse peaks. Annealing the samples at 40-102 GPa and 1500-2000 K produces new sharp Bragg reflections that can be indexed with the post-aragonite ($Pm\bar{m}n$) CaCO_3 phase [9,18] (Supplementary Fig. S1). At 105 GPa, the dominant annealing product is different and forms a new spotty pattern in the XRD images (Fig. 1), but residual

broad and diffuse reflections of precursor CaCO_3 are also present after the heating.

Crystallographic indexing of the new reflections yields monoclinic and orthorhombic solutions with unit cells consistent with the theoretical predictions of $C222_1$ [11] and $P2_1/c$ [12] CaCO_3 .

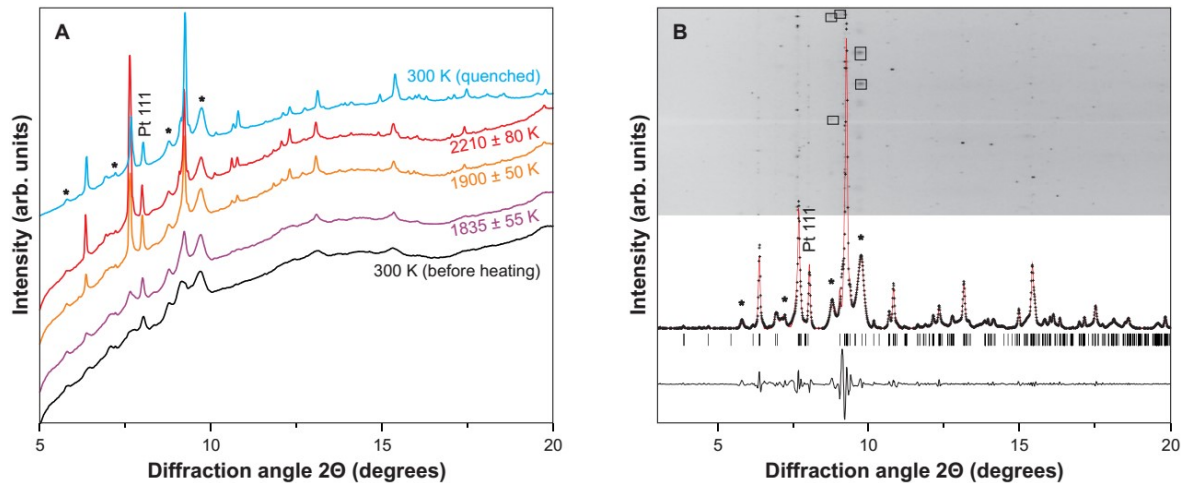


Figure 1. (A) X-ray diffraction (XRD) of CaCO_3 before, at T , and after heating at 105 GPa (with background). (B) LeBail fit of the theoretically predicted $P2_1/c$ - CaCO_3 (red line) to the experimentally observed XRD pattern (black crosses). Thin black line is the difference curve. The corresponding rectangular diffraction image is shown in the upper part of (B). Asterisks and black boxes mark some of the diffuse peaks of remnant CaCO_3 . X-ray energy is 42 keV.

Both theoretically proposed models allow indexing the new peaks yielding almost identical densities at 105 GPa ($5.01(2) \text{ g/cm}^3$). Indeed, topological analysis, performed to reveal structural differences between the two sp^3 - CaCO_3 structures, shows a high degree of similarity between the $P2_1/c$ and $C222_1$ structures with an identical atomic coordination ($\text{Ca}^{[10]}\text{C}^{[4]}\text{O}_2^{(5)}\text{O}^{(4)}$) and arrangement of Ca and C atoms. The only difference between the structures is the orientation of CO_4 -tetrahedra: all vertex-sharing helices in $C222_1$ - CaCO_3 are right-handed, while half helices in the $P2_1/c$ - CaCO_3 are left-handed (Fig. 2). Despite of these similarities, the $P2_1/c$ structure has an approximately 0.2 eV/f.u. lower enthalpy than $C222_1$ - CaCO_3 , according to the computation of Pickard and Needs [12], advocating in favor of the monoclinic structure. Here we provide further support for the $P2_1/c$ - CaCO_3 as its structural model allows indexing severely split peaks, such as the -112 and 111 Bragg reflections at ~ 7 degrees and the feature at ~ 9.2 degrees 2θ , as well as other minor reflections in the observed XRD pattern (Fig. 1B). Accordingly, LeBail refinements of the XRD patterns with the $P2_1/c$ structure systematically yield $\sim 5\%$ better fits than that performed with the $C222_1$ structure. Please note that although we could not perform a full-profile refinement in this work due to the textured XRD pattern, the observed intensities are also consistent with the $P2_1/c$ model (Supplementary Fig. S2). Hence, we confirm the prediction of the $P2_1/c$ - CaCO_3 , albeit at ~ 30 GPa higher than the theoretically predicted sp^2 - sp^3 crossover pressure [12]. We note that although $P2_1/c$ and $C222_1$ models of CaCO_3 have very

similar powder XRD patterns, their Raman spectra may bear significant differences and may help to identify the sp^3 -CaCO₃ phase.

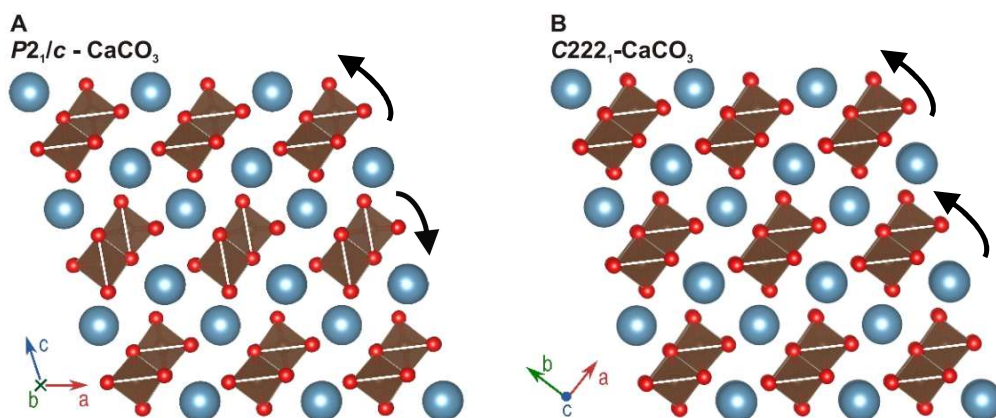


Figure 2. Structures of $P2_1/c$ -CaCO₃ (A) and $C222_1$ -CaCO₃ (B) with outlined CO₄-tetrahedra. Calcium atoms are shown in blue, carbon in brown, and oxygen in red. Black arrows show the distinct chirality of CO₄-tetrahedra chains in the crystal structures.

Depending on the probed sample area, we observed a coexistence of the post-aragonite phase with $P2_1/c$ -CaCO₃ at 103-105 GPa, which indicates that this pressure is close to the phase transition pressure. At 105 GPa and 300 K, the unit cell parameters of post-aragonite CaCO₃ are $a = 3.9360(6)$ Å, $b = 4.4372(3)$ Å, $c = 3.9049(4)$ Å ($\rho = 4.87(2)$ g/cm³), while that of $P2_1/c$ -CaCO₃ are $a = 4.5288(13)$ Å, $b = 3.3345(3)$ Å, $c = 9.0927(24)$ Å, and $\beta = 105.57(9)$ degrees ($\rho = 5.01(2)$ g/cm³) (Supplementary Table S1). The structure of sp^3 -CaCO₃ is $\sim 3\%$ denser than that of its sp^2 -bonded counterpart at 105 GPa (Fig. 3), which is larger than the previously reported density contrasts of 0.5% [19] and 1.25% [9] across the sp^2 - sp^3 transition. Importantly, the average carbon-oxygen bond length increases across the phase transition from 1.228 to 1.315 Å (by $\sim 7\%$) as a result of the increased carbon coordination. Note that in order to determine the change in C-O bond length over the sp^2 - sp^3 transition in CaCO₃ we used the experimentally refined lattice parameters of the coexisting CaCO₃ phases at 105 GPa and theoretically computed atomic positions [12]. Although we did not refine the atomic positions based on the experimental XRD, the observed intensities are consistent with the theoretically-proposed $P2_1/c$ -CaCO₃ model (Supplementary Fig. S2). Because of the increase in C-O bond length, one would expect an abrupt decrease in the frequency of the carbon-oxygen stretching vibration across the sp^2 - sp^3 transition.

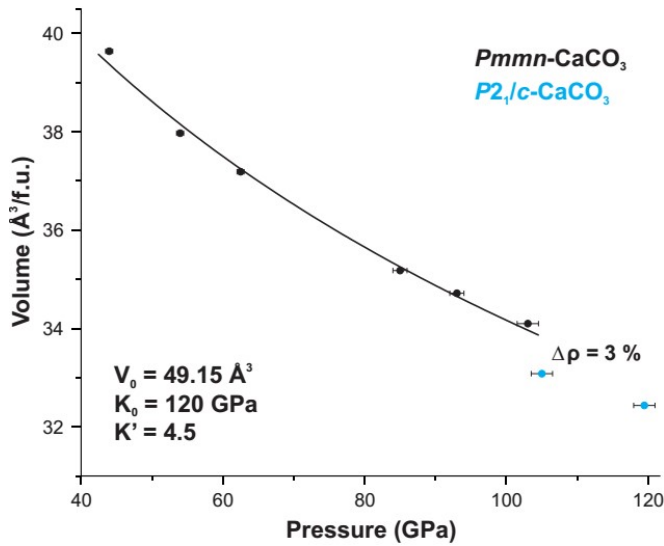


Figure 3. Pressure-volume relations for *Pmmn*-CaCO₃ (black dots) and *P2₁/c*-CaCO₃ (blue dots). Black line is a 300 K third-order Birch-Murnaghan equation of state (EOS) of *Pmmn*-CaCO₃ (post-aragonite) fitted to the collected here P-V data. Best fits were obtained using the previously reported post-aragonite V_0 value (49.15 Å³/f.u.) [18] in combination with K' in the range of 4.5-4.7. Fixing V_0 to the reported value is appropriate because of the larger number of P-V measurements in the previous study. Corresponding EOS parameters are given in the bottom left corner. Pressure uncertainty (σ) is assumed to be 0.5, 1, and 1.5 GPa for $P < 70$, 80-100, and > 100 GPa, respectively.

Raman spectroscopy. Group theory for *P2₁/c*-CaCO₃ allows 30 Raman active vibrations (15A_g + 15B_g). Raman spectra collected from the laser-heated area consistently show at least 8 new peaks all of which appear characteristic of the vibrational normal modes in the new carbonate as the frequency and relative intensity of these bands are independent of the excitation wavelength (Fig. 4). Particularly important is the new intense band at 1025 cm⁻¹. Considering the increased C-O bond length across the *sp*²-*sp*³ transition it is reasonable to suppose that this high-frequency band corresponds to the C-O stretching vibration in the CO₄-unit. We have a rough check on this assignment by assuming a harmonic oscillator and an empirically established relation of the force constant and bond length for CX compounds [32]: $f = a(r - 0.61)^{-3}$, where X is a second period element, a is a constant, and r is the C-X equilibrium bond length. Accepting the change in C-O bond length across the *sp*²-*sp*³ transition as well as the frequency of C-O symmetric stretching vibration in *sp*²-CaCO₃ at 105 GPa (1290 cm⁻¹) we obtain a frequency of 1059 cm⁻¹ for this vibration in *sp*³-CaCO₃. This is within 5 % with the observed frequency of 1025 cm⁻¹ in support of its assignment to the C-O symmetric stretching in tetrahedral-coordinated carbon. A similar comparison for the graphite-diamond C-C stretch modes yields a frequency of 1273 cm⁻¹ for the diamond T_{2g} band at 1 atm, which is again < 5 % off its actual value (1333 cm⁻¹).

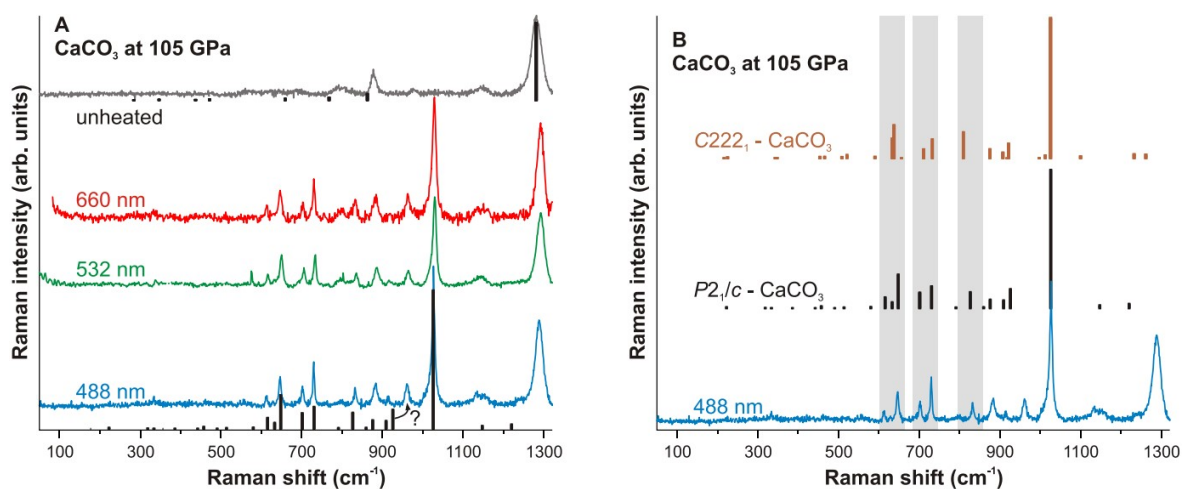


Figure 4. (A) Raman spectra of CaCO_3 at 105 GPa collected with 488, 532, and 660 nm excitations. Grey curve is the spectrum of post-aragonite CaCO_3 collected outside of the heated region. Black vertical bars are computed Raman modes of $P2_1/c$ - CaCO_3 (bottom) and post-aragonite CaCO_3 (top) corrected upwards in frequency by 1.5 % and 0.5 %, respectively. Height of the bars is proportional to the band intensity. The peak indicated by question mark deviates significantly from the $P2_1/c$ - CaCO_3 model and may be due to the unheated CaCO_3 , yet unidentified phase, or minor non-molecular CO_2 formed upon CaCO_3 thermal decomposition on Pt chunks. (B) Experimental spectrum of CaCO_3 laser-heated at 105 GPa in comparison with the theoretical spectra of $P2_1/c$ and $C222_1$ - CaCO_3 at 105 GPa as computed by LDA-DFT. Grey areas are guides to compare the computed spectra with experiment.

Furthermore, we reproduced the frequencies and intensities of all experimentally observed new Raman bands in our LDA-DFT computations of the Raman spectrum of $P2_1/c$ - CaCO_3 at 105 GPa (Supplementary Table S2). Please note that our computations systematically yielded ~ 1.5 % lower frequencies for all corresponding Raman bands observed in experiment, but when corrected for that, show a remarkable agreement with the experimental spectrum (Fig. 4). Such correction is justified because LDA-DFT yields an equilibrium volume that deviates from experimental observations by up to a few percent (*e.g.* [33]). In addition, we computed a Raman spectrum of $C222_1$ - CaCO_3 at 105 GPa (Supplementary Table S3), which, expectedly, shows a C-O vibron frequency (996 cm^{-1}) that is very close to that in $P2_1/c$ - CaCO_3 (1011 cm^{-1}). Despite this similarity, Raman bands in the $600\text{-}850 \text{ cm}^{-1}$ spectral range show subtle yet important differences between the $C222_1$ and $P2_1/c$ structures. This difference is likely due to the contrasting packing of the CO_4 -chains in the structures, which results in slightly different frequencies of deformation modes in CO_4 -units. As is clear from Figure 4B, the $P2_1/c$ model gives a better agreement with the experiment than the $C222_1$ structure, providing strong spectroscopic evidence for $P2_1/c$ - CaCO_3 at 105 GPa.

Upon decompression, we could follow the major Raman bands of sp^3 -bonded CaCO_3 down to 57 GPa (Fig. 5). The pressure-frequency dependence of these bands appears consistent with that computed for $P2_1/c$ - CaCO_3 , in support of the band assignment and product

identification. Below 57 GPa, however, we could not observe any Raman bands that can be reliably assigned to $P2_1/c$ -CaCO₃. Evidently, this indicates a full transformation to an sp^2 -bonded CaCO₃ phase below 57 GPa, as is also recorded in the intensification of the band at ~ 1200 cm⁻¹, which is representative of CO₃ groups (symmetric stretch). Identification of this phase was outside the scope of this work. We note, however, that the CaCO₃ system is rich in metastable phases (*e.g.* [16]) and it is possible that the CaCO₃ phase formed on unloading to 45 GPa is different from post-aragonite.

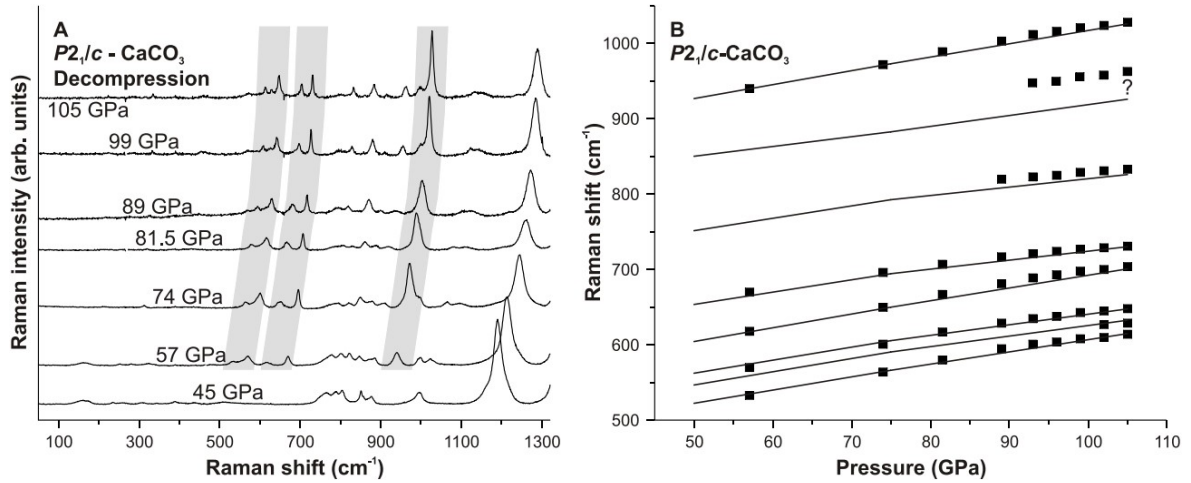


Figure 5. (A) Raman spectra ($\lambda = 488$ nm) of CaCO₃ collected on decompression after laser heating at 105 GPa. Grey areas show characteristic Raman bands of $P2_1/c$ -CaCO₃. (B) Pressure dependencies of the experimentally observed (squares) and computed (lines) Raman bands of $P2_1/c$ -CaCO₃ (frequency is corrected upwards by 1.5 %). $P2_1/c$ -CaCO₃ is preserved down to $P = 57$ GPa. The error bar for experimental measurements is not shown as it is smaller than the symbols (black squares).

Mechanism of the sp^2 - sp^3 transition in CaCO₃

To reveal the mechanism of the $Pm\bar{m}n$ -CaCO₃ \rightarrow $P2_1/c$ -CaCO₃ structural phase transition we performed variable-cell nudged elastic band (VCNEB) [34] simulations at 100 GPa, as implemented in the USPEX code [35,36]. First, we obtained an initial trajectory between the two phases using a new algorithm developed by Graf and Stevanovic (publication in preparation) to map crystal structures onto each other. The mapping algorithm relies on criteria of minimizing the total Euclidian distance between the corresponding atoms in the end structures and minimizing the change in their coordination along the map (pathway). The initial pathway was subsequently refined by the VCNEB method for the minimum-energy pathway. Both $Pm\bar{m}n \rightarrow P2_1/c$ and $P2_1/c \rightarrow Pm\bar{m}n$ paths were prepared and then optimized with VCNEB (in general, this algorithm may find different paths for forward and backward transitions), and the lowest-enthalpy path is presented in detail here. VCNEB calculations required forces and stresses, which were computed by VASP [37] at the PBE-GGA level of theory [38]. Our VCNEB calculations started with 10 intermediate images, and this number automatically increased

whenever the path became longer. Climbing image – descending image technique [39] was used to precisely locate transition states (TS) and intermediate minima (corresponding to potential metastable intermediate phases (IP)). Spring constants varied from 3 to 6 eV/Å². VCNEB calculations were run for 1000 steps, enabling accurate and well-converging results. At the pressure of 100 GPa, *P2₁/c*-CaCO₃ phase is more stable by 0.02 eV/atom than post-aragonite. The barrier height is quite large, 0.14 eV/atom (or 0.70 eV/f.u.), implying that this transition is kinetically feasible only at high temperatures, in agreement with experimental results of this work.

One important distinction between the crystal structures of *sp*²- and *sp*³-CaCO₃ is that CO₃ groups in post-aragonite are isolated while CO₄ groups in *P2₁/c*-CaCO₃ are corner-linked into pyroxene-like chains. Accordingly, the transformation mechanism is quite complex and can be divided into four stages (Fig. 6): each stage corresponds to an energy minimum, and boundaries between them correspond to transition states (TS). In the first stage of the transformation, the post-aragonite structure distorts gradually with all CO₃-triangles becoming non-planar. This distortion becomes critical at transition state #1 (TS₁) triggering the second stage of the transition with all carbon atoms forming additional bonds with oxygen atoms of the next layer, stitching isolated CO₃-groups into infinite chains of CO₄-tetrahedra. This topology corresponds to a local enthalpy minimum and has a *P2₁* symmetry (intermediate phase #1, IP₁). However, the enthalpy minimum of IP₁ is very shallow (Fig. 6). Towards the transition state TS₂, one of the C-O bonds of the original CO₃-triangle gradually elongates and eventually breaks. In the third stage, between the transition states TS₂ and TS₃, yet another metastable structure with a *P2₁* symmetry appears, featuring flat and non-coplanar CO₃-triangles and a shallow enthalpy minimum. As this structure distorts towards the transition state TS₃, carbonate triangles reorient, nearby oxygens displace towards them, and eventually one obtains infinite chains of CO₄-tetrahedra in the same topology as in the *P2₁/c* structure. The final, fourth, stage of the transformation is just a relaxation towards the theoretically predicted *P2₁/c*-CaCO₃ structure [12].

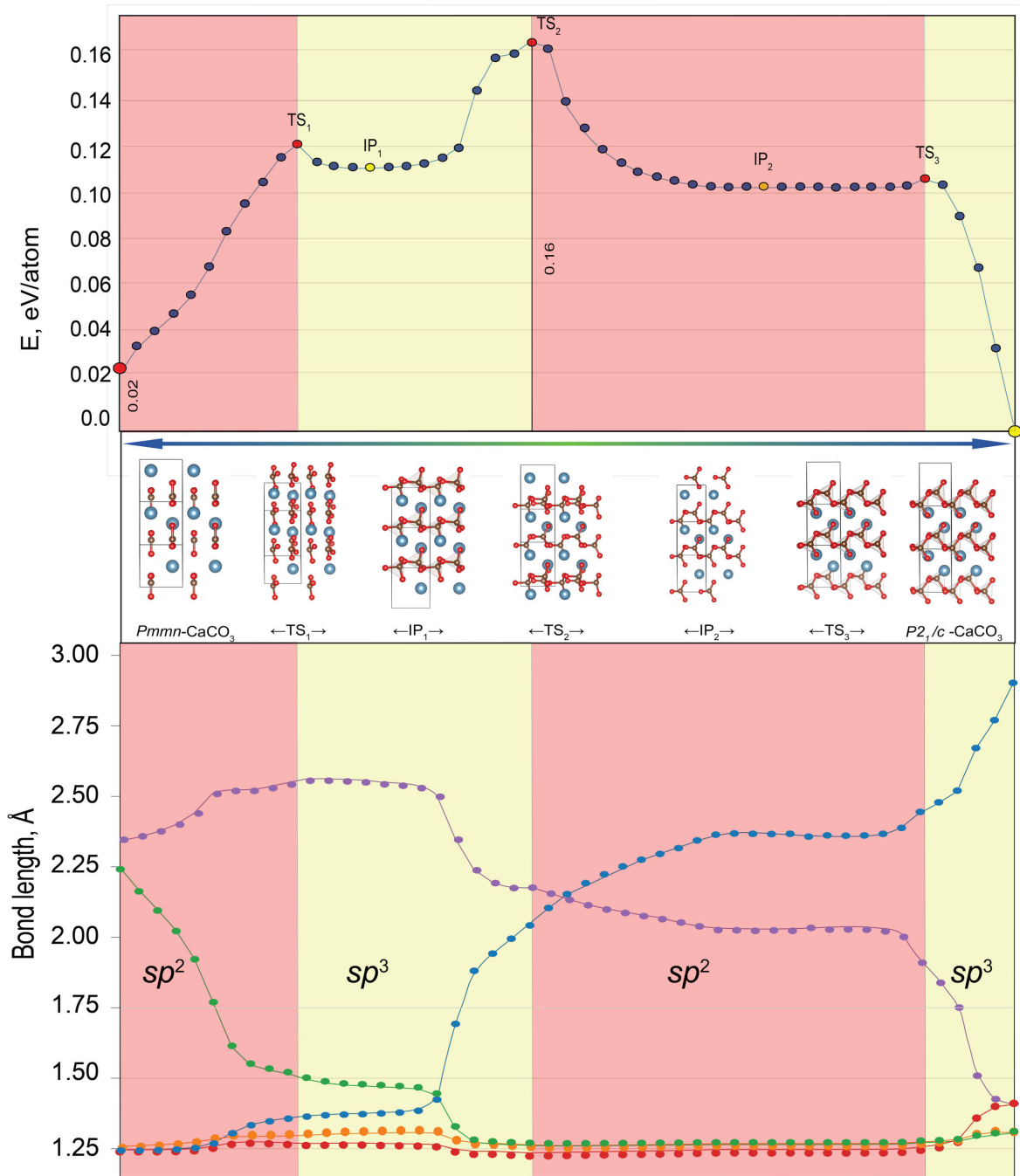


Figure 6. Mechanism of the $Pmmn$ (post-aragonite) $\rightarrow P2_1/c$ transition of $CaCO_3$ at 100 GPa. Structures of initial post-aragonite phase, transition states TS_1 , TS_2 and TS_3 , intermediate phases IP_1 , IP_2 and final $P2_1/c$ of $CaCO_3$ are shown (for clarity, we highlighted CO_4 -tetrahedra). The evolution of five shortest C-O distances is shown across the proposed transition path.

Transition states define the crossover between different topologies – *i.e.* the point at which chemical bonds are formed or broken. It is very tempting to think of some maximum bond lengths characteristic of a given pair of atoms (*e.g.* C-O), beyond which bonds break. However, our results show this not to be the case as the values of critical C-O bond lengths vary for

different transitions. This suggests that the phase transitions are driven not just by the nearest-neighbor interactions, but longer-range interactions and cooperative effects are important.

Three fundamental comments are due regarding the mechanism of this phase transition. First, the intermediate minima (IP₁ and IP₂) in this case are so shallow that they are unlikely to be quenched in the experiment: these minima are not strongly kinetically protected and will rapidly decay into post-aragonite or $P2_1/c$, respectively. The role of these intermediate minima is to be “stepping stones” on the transition pathway, lowering the overall barrier. This is in contrast with the case of BH, a newly predicted compound, where the phase transition involved a very deep and most likely experimentally obtainable, intermediate phase [40]. Second, the transition mechanism discussed here is the best mechanism that we could find (*i.e.* with the lowest activation enthalpy). However, as we did not perform an exhaustive search over transition paths, we cannot rule out the possibility of other mechanisms. At the moment, there is no algorithm for predicting globally optimal transition pathway, even within the mean-field picture. Third, the mechanism we just presented is based on the mean-field picture with all unit cells undergoing the same evolution at a given time. In reality, phase transitions occur via nucleation and growth; thus, the mean-field approach access crude but crystallographically and intuitively tractable models. Full exploration of nucleation and growth phenomena requires very large systems (with 10^2 - 10^4 atoms) and advanced sampling techniques, such as transition path sampling (*e.g.* [41]); we refer the reader to our recent works employing this methodology (also implemented in the USPEX code) [42,43] and note that such simulations require an accurate forcefield and at the *ab initio* level of theory are computationally unaffordable at the moment.

Experimental evidence for sp^3 -bonded carbonates

Identification of sp^3 -bonded carbonates solely based on XRD is problematic as it requires precise structure determination, which is often challenging at high pressure. Most previous reports on sp^3 -carbonates in MgCO₃ and FeCO₃ systems relied on LeBail-type fits of theoretically predicted structures to experimentally observed power-like XRD patterns. For example, Ref. [44] have reported sp^3 -MgCO₃ at $P \sim 80$ GPa and $T \sim 2000$ K based on the match of XRD to the theoretical prediction of Ref. [11]. One notable exception is the report of Mg₂Fe₂C₄O₁₃ with tetrahedrally-coordinated carbon at 135 GPa [45] with single-crystal structure solution methods applied to a multi-grain sample synthesized in the (Mg,Fe)CO₃ system. We summarize previous experimental reports on sp^3 -carbonates in the Table 1.

Table 1. Summary of experimental reports on carbonates with tetrahedrally-coordinated carbon.

References	System	Space group	P, GPa	Problems
Ref. [19]	CaCO ₃	$C222_1$	130	No spectroscopic probe for sp^3 -carbon
Ref. [44]	MgCO ₃	$C2/m$ and	82	LeBail fit, no spectroscopic probe for sp^3 -carbon

		$P2_1/a$		
Ref. [46]	FeCO ₃	-	80	LeBail fit; no spectroscopic probe for sp^3 -carbon
Ref. [47]	(Mg,Fe)CO ₃	$C2/m$ and $P2_1/a$	80	LeBail fit
Ref. [45]	(Mg,Fe)CO ₃	$C2/c$	135	No spectroscopic probe for sp^3 -carbon

Unlike XRD, vibrational spectroscopy provides bonding fingerprints of the material and is particularly sensitive to the carbon hybridization and chemical environment (*e.g.* [48]). As such, Raman and/or infrared spectroscopy provide independent evidence for tetrahedrally-coordinated carbon and must be used together with crystallographic probes for a reliable identification of sp^3 -carbonates in high-pressure experiments. Realizing weaknesses of XRD probes in identifying the bond character, Boulard et al., [47] reported on synchrotron infrared absorption experiments in (Mg_{0.25}Fe_{0.75})CO₃ at 80 GPa, noting a new band that is characteristic of the C-O asymmetric stretching vibration in CO₄-groups. The band assignment relied on first-principles calculations of the infrared spectrum of sp^3 -MgCO₃ ($P2_1/a$ space group). However, other theoretically predicted bands were not fully assigned in the experiment [47].

In contrast to previous studies, here we provided strong spectroscopic evidence of sp^3 -carbonates. Specifically, the intense Raman band at $\sim 1025 \text{ cm}^{-1}$ (at 105 GPa) and its pressure dependence ($\sim 1.8 \text{ cm}^{-1}/\text{GPa}$) in $P2_1/c$ -CaCO₃ are characteristic of the symmetrical stretching vibration in its CO₄-groups. In principle, these spectroscopic features can be used in future studies of sp^3 -carbonates at high pressure to confirm fourfold carbon coordination.

Our results are also important to validate density functionals used in crystal structure predictions. Pickard and Needs [12] noted that Perdew-Burke-Ernzerhof generalized gradient approximation (PBE-GGA) and local density approximation (LDA) yield essentially similar transition pressures, and thus, provide accurate description of the electronic structures. Here we identified the sp^3 -CaCO₃ phase and the sp^2 - sp^3 crossover pressure (105 GPa), which appears to be $\sim 30 \text{ GPa}$ higher than the theoretically predicted transition pressure of 76 GPa (at 0 K), suggesting that the entropy term in the free energy is substantial. We showed that high temperature is required to overcome the kinetic barriers associated with the sp^2 - sp^3 transition, indicating that complex energy landscapes are typical not only of pure carbon but of carbonates just as well. As a result, a variety of metastable sp^2 -CaCO₃ polymorphs have been observed at $P < 40 \text{ GPa}$ [16]. Results of this study suggest that sp^3 -CaCO₃ may also have a number of metastable structures accessible through compression without high-T annealing. In this regard, the Raman signature of sp^3 -carbonates may come in useful to diagnose tetrahedrally-coordinated carbon.

Geochemical and geophysical implications of sp^3 -carbonates in the lowermost mantle

The equilibrium composition of mantle carbonates is governed by the chemical reactions with surrounding minerals [13,14,49] and thermodynamic stability of corresponding carbonate phases. Due to the chemical interaction with pyroxene or bridgmanite in the mantle, CaCO_3 transforms to Fe-bearing magnesite (up to 10 % Fe [50]) at 2-80 GPa [51-54] despite several phase transitions in sp^2 - CaCO_3 which can modify the chemical equilibrium in this pressure range [9,12]. Also, the spin transition in Fe-bearing MgCO_3 at $P \sim 45$ GPa may promote iron solubility in the carbonate phase due to crystal field effects [55] and ionic size similarity of low spin Fe^{2+} with Mg^{2+} [56], but this has never been quantitatively addressed in experiment. The sp^2 - sp^3 transition in MgCO_3 at $P \sim 80$ GPa further upholds the Mg-rich carbonate composition, as revealed by a computation of enthalpies in the reaction $\text{MgCO}_3 + \text{CaSiO}_3 = \text{CaCO}_3 + \text{MgSiO}_3$ as a function of pressure and accounting for phase transitions [11,12]. The theoretically predicted sp^2 - sp^3 transition in CaCO_3 at 76 GPa eventually stabilizes CaCO_3 against MgCO_3 at $P > \sim 100$ GPa [12]. Here we have synthesized the predicted $P2_1/c$ - CaCO_3 at $P \sim 105$ GPa and $T \sim 2000$ K, about 30 GPa higher than the theoretically predicted sp^2 - sp^3 transition pressure at 0 K. Taking into account this 30 GPa discrepancy we propose that the crossover to Ca-carbonates in Earth (*i.e.* at high temperature) may be expected at $P \sim 135$ GPa, which corresponds to the pressure at the core-mantle boundary. This inference can be tested via high-pressure studies of chemical reactions in mechanical mixtures of MgCO_3 with CaSiO_3 or CaCO_3 with MgSiO_3 at high pressure and temperature.

Conclusions

In summary, we located the sp^2 - sp^3 transition in CaCO_3 and identified the $P2_1/c$ - CaCO_3 at $P > 105$ GPa using x-ray diffraction and Raman spectroscopy. Using first-principles methods, we showed that the mechanism of the sp^2 - sp^3 crossover in CaCO_3 involves several intermediate phases with sp^2 and sp^3 bonding motifs. Finally, our results support the idea of the crossover in the carbonate crystal chemistry that leads to Ca-rich carbonates at the base of the mantle.

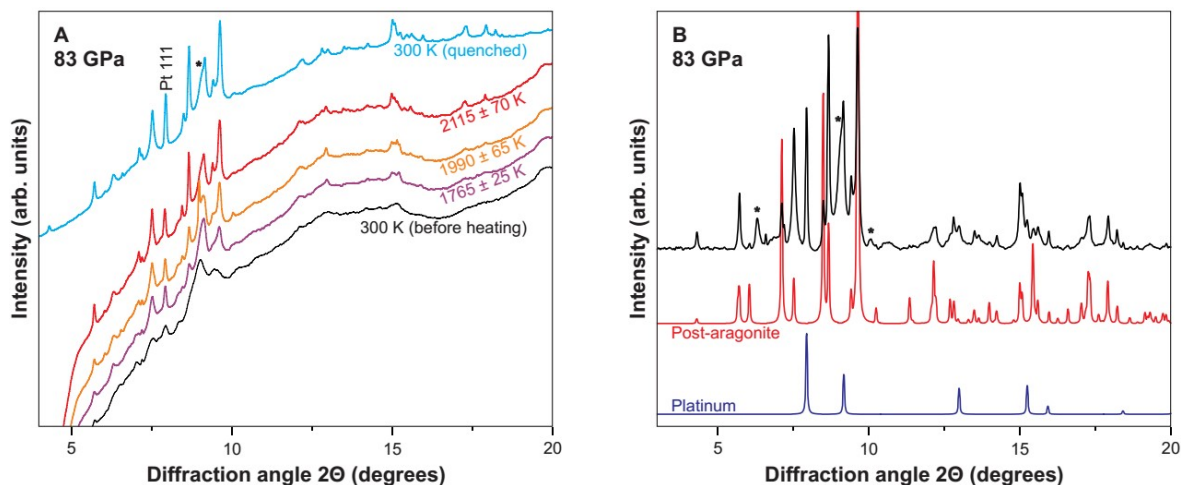
Acknowledgments

This work was supported by the National Science foundation, grants NSF EAR/IF 1531583, NSF EAR-1520648 and NSF EAR/IF-1128867, the Army Research Office (56122-CH-H), the Carnegie Institution of Washington and Deep Carbon Observatory. S.S.L. was partly supported by state assignment project No. 0330-2014-0013. Portions of this work were performed at GeoSoilEnviroCARS (The University of Chicago, Sector 13), Advanced Photon Source (APS), Argonne National Laboratory. GeoSoilEnviroCARS is supported by the National

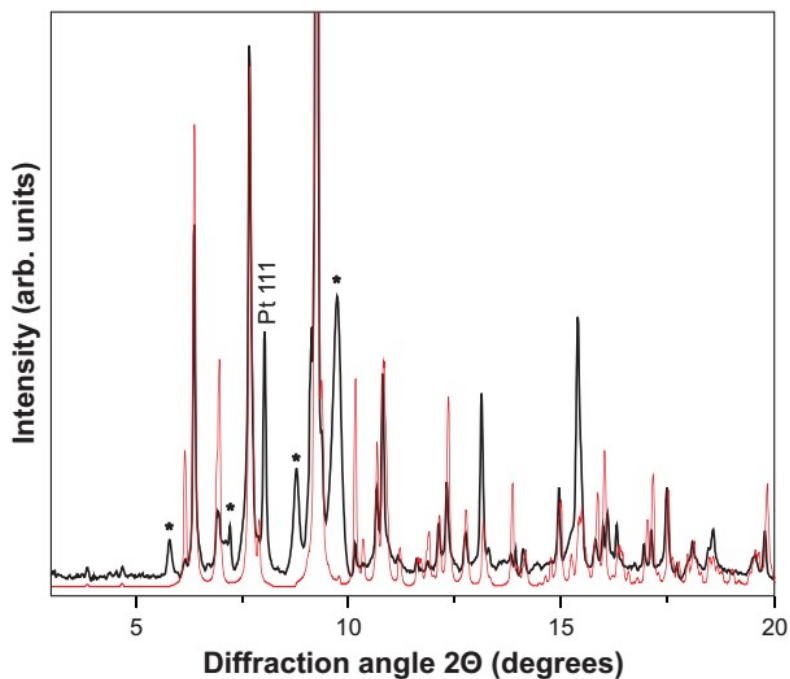
Science Foundation - Earth Sciences (EAR-1128799) and Department of Energy- GeoSciences (DE-FG02-94ER14466). This research used resources of the Advanced Photon Source, a U.S. Department of Energy (DOE) Office of Science User Facility operated for the DOE Office of Science by Argonne National Laboratory under Contract No. DE-AC02-06CH11357. We thank Dr. E. V. Alexandrov for his assistance in topological analysis. P.N.G. was supported by the Ministry of Education and Science of Russian Federation (No 14.B25.31.0032 and MK-3417.2017.5). A. F. G. was partly supported by the Chinese Academy of Sciences visiting professorship for senior international scientists (Grant No. 2011T2J20), Recruitment Program of Foreign Expert, the National Natural Science Foundation of China (grant number 21473211), and the Chinese Academy of Sciences (grant number YZ201524). A.R.O was supported by Russian Science Foundation (grant 16-13-10459).

SUPPLEMENTARY INFORMATION

Supplementary Figures



Supplementary Figure S1. (A) X-ray diffraction (XRD) of CaCO_3 before, at T , and after heating at 83 GPa (with background). (B) Background-subtracted XRD pattern (black line) of the heated CaCO_3 at 83 GPa after cooling to 300 K. Red and blue lines are powder XRD patterns of post-aragonite CaCO_3 and Pt, respectively. Asterisks and black boxes mark some of the diffuse peaks of remnant CaCO_3 . X-ray energy is 42 keV.



Supplementary Figure S2. Room-temperature x-ray diffraction (XRD) of CaCO_3 laser-heated at 105 GPa (black line) in comparison to the powder XRD pattern of the $P2_1/c$ - CaCO_3 model [12] (red line). Asterisks and black boxes mark some of the diffuse peaks of remnant CaCO_3 . X-ray energy is 42 keV.

Supplementary Tables

Supplementary Table S1. Lattice parameters of the $P2_1/c$ -, $C222_1$ -, and $Pmmn$ - CaCO_3 models as refined from the experimental XRD data at 105 GPa.

Model / Lattice parameter	a, Å	b, Å	c, Å	β , degrees
$P2_1/c$ - CaCO_3	4.5288(13)	3.3345(3)	9.0927 (24)	105.57(9)
$C222_1$ - CaCO_3	5.5057(4)	7.2389(3)	3.3425(2)	-
$Pmmn$ - CaCO_3	3.9360(6)	4.4372(3)	3.9049(4)	-

Supplementary Table S2. Vibrational properties of $P2_1/c$ - CaCO_3 at 105 GPa as computed by LDA-DFT.

Mode #	Frequency (cm^{-1})	Frequency (THz)	IR intensity	Raman intensity	Depolarization factor
1	0	0	0	0	0.2089
2	0	0	0	0	0.4892
3	0	0	0	0	0.2933
4	173.5	5.2014	0	0.0201	0.75
5	208.52	6.2513	0.1822	0	0.7023
6	218.25	6.5431	0	1.033	0.7203
7	273.91	8.2116	0.4094	0	0.232
8	312.96	9.3823	0	0.3429	0.2483
9	313.87	9.4095	0	0.0932	0.75
10	328.24	9.8403	0	0.2048	0.0856
11	350.07	10.4947	0	0.0345	0.75
12	370.5	11.1073	0.0593	0	0.6904
13	379.49	11.3767	0	0.1724	0.7051
14	435.31	13.0502	0	0.1706	0.75
15	441.23	13.2278	20.9243	0	0.7494
16	441.67	13.241	0.0312	0	0.7499
17	449.89	13.4875	0	1.9539	0.7496
18	482.54	14.4661	0	0.1497	0.75
19	484.64	14.5292	11.2104	0	0.6888
20	494.59	14.8276	3.9715	0	0.612
21	505.47	15.1535	0	0.9328	0.75
22	514.42	15.4218	10.1563	0	0.7457
23	570.83	17.1132	0	1.2989	0.3694
24	576.9	17.2951	0.0496	0	0.7068
25	589.19	17.6636	9.0206	0	0.6326
26	605.96	18.1662	0	10.0644	0.75
27	623.51	18.6923	0	5.5571	0.2656
28	623.74	18.6991	6.3122	0	0.2648
29	638.35	19.1374	0	31.0868	0.75
30	652.25	19.554	0.2032	0	0.7494
31	656.42	19.679	0.0026	0	0.6994
32	690.65	20.7052	0	14.3927	0.3381
33	718.39	21.5367	0.2715	0	0.7481
34	719.63	21.574	0	20.1884	0.7439
35	779.3	23.3628	0	0.7965	0.0637
36	784.68	23.5243	63.689	0	0.5959
37	797.73	23.9155	9.5441	0	0.7248
38	814.05	24.4045	0	14.9039	0.75
39	840.02	25.1833	1.5425	0	0.7233

40	847.03	25.3932	0	1.1494	0.75
41	863.18	25.8775	0	8.0109	0.75
42	890.86	26.7074	0.6486	0	0.5888
43	895.47	26.8454	0	7.2391	0.6332
44	897.97	26.9205	21.9671	0	0.6424
45	905.2	27.1371	0.0535	0	0.3265
46	912.41	27.3534	0	17.7336	0.1821
47	1000.57	29.9963	2.546	0	0.0103
48	1011.05	30.3105	0	127.1435	0.0079
49	1131.01	33.9068	0	2.7042	0.75
50	1138.17	34.1214	26.799	0	0.195
51	1202.25	36.0425	0	4.02	0.75
52	1223.71	36.6859	20.4645	0	0.7365
53	1332.78	39.9558	83.6266	0	0.7498
54	1332.91	39.9597	0	11.085	0.75
55	1409.66	42.2605	6.1204	0	0.1223
56	1413.35	42.3713	0	10.0924	0.1273
57	1435.07	43.0223	0	9.4744	0.5871
58	1483.68	44.4796	31.1199	0	0.6671
59	1514.84	45.4137	0	6.546	0.75
60	1553.62	46.5763	77.3633	0	0.6603

Supplementary Table S3. Vibrational properties of C222₁-CaCO₃ at 105 GPa as computed by LDA-DFT.

Mode #	Frequency (cm ⁻¹)	Frequency (THz)	IR intensity	Raman intensity	Depolarization factor
1	0	0	0	0	0.75
2	0	0	0	0	0.75
3	0	0	0	0	0.75
4	210.03	6.2965	0.0381	0.0984	0.75
5	218.23	6.5422	0.3481	0.897	0.75
6	240.1	7.1981	0.0003	0.0009	0.75
7	283.81	8.5085	0.0003	0	0.75
8	300.14	8.9979	0.0011	0.0001	0.75
9	332.6	9.971	0.0067	0.0004	0.75
10	332.76	9.9758	0	0.2009	0.3151
11	337.47	10.117	4.9077	0.2023	0.75
12	384.49	11.5267	0.0002	0	0.75
13	426.34	12.7813	0.003	0.007	0.75
14	440.45	13.2045	0.2366	1.3334	0.75
15	440.88	13.2173	0	0	0.0173
16	447.78	13.424	0.0002	0	0.75
17	451.93	13.5484	26.8854	1.4425	0.75
18	492.49	14.7646	0.007	0.002	0.75
19	493.73	14.8016	1.6703	1.2386	0.75
20	494.17	14.8149	24.4814	0.0016	0.75
21	505.86	15.1653	4.21	3.3619	0.75
22	551.35	16.5291	0.0016	0.004	0.75
23	573.24	17.1853	1.0609	1.4055	0.75
24	591.76	17.7407	0	0.0077	0.75
25	614.79	18.431	0	19.6013	0.1583
26	619.09	18.5598	0.3029	32.9517	0.75

27	637.15	19.1011	0	0.0461	0.1472
28	647.29	19.4053	0.0003	0.0009	0.75
29	664.14	19.9103	0.2501	0.0001	0.75
30	677.8	20.3198	0.002	0.0058	0.75
31	690.38	20.6971	0	8.9335	0.426
32	707.62	21.2139	0	0.0006	0.6001
33	711.42	21.328	0.0307	18.7983	0.75
34	731.82	21.9395	0	0.0016	0.75
35	770.74	23.1062	0	0	0.75
36	786.02	23.5643	11.699	25.9228	0.75
37	806.61	24.1816	0.0186	0.0258	0.75
38	849.79	25.476	2.8018	9.0094	0.75
39	854.1	25.6051	0.0003	0.0029	0.75
40	871.31	26.1212	0.0174	0.0021	0.75
41	871.95	26.1403	0.0003	0.0038	0.75
42	881.15	26.4161	1.1213	5.6692	0.75
43	890.97	26.7107	10.9965	0.0472	0.75
44	894.9	26.8286	0	14.5087	0.2294
45	921.24	27.6181	0	0.0121	0.1111
46	968.82	29.0443	0	0.2781	0.0056
47	983.24	29.4767	62.6936	2.8823	0.75
48	995.72	29.851	0	140.0152	0.0075
49	1068.34	32.0279	50.9045	1.9079	0.75
50	1086.84	32.5827	0.0089	0.0006	0.75
51	1171.28	35.1141	0.0024	0.0004	0.75
52	1196.96	35.884	18.9827	4.0087	0.75
53	1225.34	36.7348	51.9147	3.6436	0.75
54	1245.1	37.3273	0.0073	0.0007	0.75
55	1360.03	40.7727	0.0007	0	0.75
56	1384.76	41.5141	0	7.461	0.0958
57	1416.35	42.4612	0	0.0002	0.0266
58	1459.06	43.7415	60.2865	0.1559	0.75
59	1480.42	44.3819	73.8631	6.3651	0.75
60	1560.12	46.7711	0.0009	0	0.75

Supplementary Table S4. Vibrational properties of *Pmmn*-CaCO₃ (post-aragonite) at 105 GPa as computed by LDA-DFT.

Mode #	Frequency (cm ⁻¹)	Frequency (THz)	IR intensity	Raman intensity	Depolarization factor
1	0	0	0	0	0.3095
2	0	0	0	0	0.75
3	0	0	0	0	0.7498
4	239.85	7.1904	0	0.5682	0.75
5	283.97	8.5133	0.0002	1.5292	0.75
6	297.49	8.9184	0	0.0017	0.75
7	346.56	10.3895	0	4.0606	0.3295
8	394.89	11.8385	7.3676	0.0004	0.75
9	395.67	11.8619	15.3288	0.0024	0.75
10	397.69	11.9225	0.0005	0.2161	0.75
11	437.17	13.106	0	2.5285	0.3858
12	471.65	14.1398	0.0416	5.4371	0.75

13	529.91	15.8862	4.9378	0.0025	0.75
14	585.31	17.5472	1.101	0.0543	0.75
15	602.08	18.0498	12.7315	0.0001	0.0186
16	630.88	18.9133	0.0013	0.3585	0.75
17	659.19	19.7621	0	7.7721	0.75
18	719.49	21.5697	0.0015	0.0148	0.75
19	767.97	23.0232	0.3733	13.1236	0.75
20	775.94	23.262	9.113	0.5664	0.75
21	803.67	24.0933	9.9435	0.0095	0.75
22	813.64	24.3923	0.492	0.1354	0.75
23	862.85	25.8677	0.002	29.4427	0.4727
24	870.63	26.1009	2.6172	0.0299	0.4034
25	1281.13	38.4072	0.0018	350.143	0.0192
26	1291.31	38.7125	0.2826	1.5192	0.0179
27	1652.68	49.546	71.9921	0	0.75
28	1664.4	49.8973	0.0002	14.2517	0.7026
29	1738.5	52.1191	0	0.5207	0.75
30	1840.75	55.1843	61.7667	0.0002	0.0952

References

- [1] F. P. Bundy, W. A. Bassett, M. S. Weathers, R. J. Hemley, H. K. Mao, and A. F. Goncharov, *Carbon* **34**, 141 (1996).
- [2] J. E. Field, *The Properties of natural and synthetic diamond* (Academic Press, London ; San Diego, 1992).
- [3] V. D. Blank, S. G. Buga, G. A. Dubitsky, N. R. Serebryanaya, M. Y. Popov, and B. Sundqvist, *Carbon* **36**, 319 (1998).
- [4] Y. Lin, L. Zhang, H. K. Mao, P. Chow, Y. M. Xiao, M. Baldini, J. F. Shu, and W. L. Mao, *Phys. Rev. Lett.* **107**, 175504 (2011).
- [5] R. C. Powles, N. A. Marks, D. W. M. Lau, D. G. McCulloch, and D. R. McKenzie, *Carbon* **63**, 416 (2013).
- [6] A. A. Godovikov, *Mineralogiia* (Nedra, Moskva, 1975).
- [7] F. Liebau, *Structural chemistry of silicates : structure, bonding, and classification* (Springer-Verlag, Berlin ; New York, 1985).
- [8] N. V. Skorodumova, A. B. Belonoshko, L. Huang, R. Ahuja, and B. Johansson, *Am. Mineral.* **90**, 1008 (2005).
- [9] A. R. Oganov, C. W. Glass, and S. Ono, *Earth. Planet. Sci. Lett.* **241**, 95 (2006).
- [10] S. Arapan, J. S. De Almeida, and R. Ahuja, *Phys. Rev. Lett.* **98**, 268501 (2007).
- [11] A. R. Oganov, S. Ono, Y. M. Ma, C. W. Glass, and A. Garcia, *Earth. Planet. Sci. Lett.* **273**, 38 (2008).
- [12] C. J. Pickard and R. J. Needs, *Phys Rev B* **91**, 104101 (2015).
- [13] I. Martinez, J. Z. Zhang, and R. J. Reeder, *Am. Mineral.* **81**, 611 (1996).
- [14] K. Sato and T. Katsura, *Earth. Planet. Sci. Lett.* **184**, 529 (2001).
- [15] K. Catalli and Q. Williams, *Am. Mineral.* **90**, 1679 (2005).
- [16] M. Merlini, M. Hanfland, and W. A. Crichton, *Earth. Planet. Sci. Lett.* **333**, 265 (2012).
- [17] T. Pippinger, R. Miletich, M. Merlini, P. Lotti, P. Schouwink, T. Yagi, W. A. Crichton, and M. Hanfland, *Phys. Chem. Miner.* **42**, 29 (2015).
- [18] S. Ono, T. Kikegawa, Y. Ohishi, and J. Tsuchiya, *Am. Mineral.* **90**, 667 (2005).
- [19] S. Ono, T. Kikegawa, and Y. Ohishi, *Am. Mineral.* **92**, 1246 (2007).
- [20] N. C. Holmes, J. A. Moriarty, G. R. Gathers, and W. J. Nellis, *J. Appl. Phys.* **66**, 2962 (1989).
- [21] V. B. Prakapenka, A. Kubo, A. Kuznetsov, A. Laskin, O. Shkurikhin, P. Dera, M. L. Rivers, and S. R. Sutton, *High Pressure Res.* **28**, 225 (2008).

- [22] C. Prescher and V. Prakapenka, *High Pressure Res.*, DOI: 10.1080/08957959.2015.1059835 (2015).
- [23] B. H. Toby, *J. Appl. Crystallogr.* **34**, 210 (2001).
- [24] A. C. Larson and R. B. Von Dreele, Los Alamos National Laboratory Report LAUR 86-748 (2004).
- [25] J. Gonzalez-Platas, M. Alvaro, F. Nestola, and R. Angel, *J. Appl. Crystallogr.* **49**, 1377 (2016).
- [26] K. Momma and F. Izumi, *J. Appl. Crystallogr.* **44**, 1272 (2011).
- [27] Y. Akahama and H. Kawamura, *J. Appl. Phys.* **100** (2006).
- [28] P. Giannozzi *et al.*, *J Phys-Condens Mat* **21** (2009).
- [29] D. R. Hamann, M. Schluter, and C. Chiang, *Phys. Rev. Lett.* **43**, 1494 (1979).
- [30] D. M. Ceperley and B. J. Alder, *Phys. Rev. Lett.* **45**, 566 (1980).
- [31] H. J. Monkhorst and J. D. Pack, *Phys Rev B* **13**, 5188 (1976).
- [32] E. Kurita, H. Matsuura, and K. Ohno, *Spectrochim Acta A* **60**, 3013 (2004).
- [33] H. Hsu, K. Umemoto, M. Cococcioni, and R. M. Wentzcovitch, *Phys. Earth Planet. Inter.* **185**, 13 (2011).
- [34] G. R. Qian, X. Dong, X. F. Zhou, Y. J. Tian, A. R. Oganov, and H. T. Wang, *Comput. Phys. Commun.* **184**, 2111 (2013).
- [35] A. R. Oganov and C. W. Glass, *J. Chem. Phys.* **124** (2006).
- [36] A. O. Lyakhov, A. R. Oganov, H. T. Stokes, and Q. Zhu, *Comput. Phys. Commun.* **184**, 1172 (2013).
- [37] G. Kresse and J. Furthmuller, *Phys Rev B* **54**, 11169 (1996).
- [38] J. P. Perdew, K. Burke, and M. Ernzerhof, *Phys. Rev. Lett.* **77**, 3865 (1996).
- [39] G. Henkelman, B. P. Uberuaga, and H. Jonsson, *J. Chem. Phys.* **113**, 9901 (2000).
- [40] C. H. Hu, A. R. Oganov, Q. Zhu, G. R. Qian, G. Frapper, A. O. Lyakhov, and H. Y. Zhou, *Phys. Rev. Lett.* **110**, 165504 (2013).
- [41] P. G. Bolhuis, D. Chandler, C. Dellago, and P. L. Geissler, *Annu. Rev. Phys. Chem.* **53**, 291 (2002).
- [42] S. E. Boulfelfel, A. R. Oganov, and S. Leoni, *Sci Rep-Uk* **2** (2012).
- [43] B. X. Li, G. R. Qian, A. R. Oganov, S. E. Boulfelfel, and R. Faller, *J. Chem. Phys.* **146** (2017).
- [44] E. Boulard, A. Gloter, A. Corgne, D. Antonangeli, A. L. Auzende, J. P. Perrillat, F. Guyot, and G. Fiquet, *Proc. Natl. Acad. Sci. U.S.A.* **108**, 5184 (2011).
- [45] M. Merlini, M. Hanfland, A. Salamat, S. Petitgirard, and H. Muller, *Am. Mineral.* **100**, 2001 (2015).
- [46] E. Boulard *et al.*, *J Geophys Res-Sol Ea* **117**, B02208 (2012).
- [47] E. Boulard, D. Pan, G. Galli, Z. X. Liu, and W. L. Mao, *Nat. Commun.* **6** (2015).
- [48] E. Stavrou, S. Lobanov, H. F. Dong, A. R. Oganov, V. B. Prakapenka, Z. Konopkova, and A. F. Goncharov, *Chem. Mater.* **28**, 6925 (2016).
- [49] J. A. Dalton and B. J. Wood, *Earth. Planet. Sci. Lett.* **119**, 511 (1993).
- [50] V. Stagno, Y. Tange, N. Miyajima, C. A. McCammon, T. Irifune, and D. J. Frost, *Geophys Res Lett* **38**, L19309 (2011).
- [51] I. Kushiro, H. Satake, and S. Akimoto, *Earth. Planet. Sci. Lett.* **28**, 116 (1975).
- [52] G. Brey, W. R. Brice, D. J. Ellis, D. H. Green, K. L. Harris, and I. D. Ryabchikov, *Earth. Planet. Sci. Lett.* **62**, 63 (1983).
- [53] C. Biellmann, P. Gillet, F. Guyot, J. Peyronneau, and B. Reynard, *Earth. Planet. Sci. Lett.* **118**, 31 (1993).
- [54] Y. Seto, D. Hamane, T. Nagai, and K. Fujino, *Phys. Chem. Miner.* **35**, 223 (2008).
- [55] S. S. Lobanov, A. F. Goncharov, and K. D. Litasov, *Am. Mineral.* **100**, 1059 (2015).
- [56] B. Lavina, P. Dera, R. T. Downs, V. Prakapenka, M. Rivers, S. Sutton, and M. Nicol, *Geophys Res Lett* **36**, L23306 (2009).